J. Fluid Mech. (1983), *vol.* 129, *pp.* 385–407
Printed in Great Britain

Barge motions in random seas – a comparison of theory and experiment

By D. T. BROWN, R. EATOCK TAYLOR AND M. H. PATEL
London Centre for Marine Technology, Department of Mechanical Engineering, University College London

(Received 20 June 1982)

This paper describes a comparison of experimental data and theoretical results for the motions in waves of large flat-bottomed barges having zero forward speed. The experimental data are derived from model tests at two scales (1 : 36 and 1 : 108). These consist of measurements of motions in surge, sway, heave, roll, pitch and yaw to long-crested seas approaching the barge models at two orientation angles (head and beam seas). The experimental data are compared with results computed from linearized potential-flow theory, which accounts for the diffraction and radiation of gravity waves around the barge. The boundary-integral scheme employed to solve this potential-flow problem is briefly reviewed.

The experimental data at two scales and the theoretical results show that potential-flow theory is in reasonable agreement with experimental data for all motions except roll near resonance. These roll-motion discrepancies, due to vortex shedding from bilge-keel edges, are discussed. Some of the observable effects of scale in the model tests are highlighted.

1. Introduction

Large ocean-going flat-bottomed barges are commonly used in the offshore oil industry for the transportation of structures and other large cargoes. The wave-induced motion response of these barges is an important feature which governs their utility, since the cargo and sea fastenings have to be stressed to withstand the resultant inertial forces. In some cases, particularly for roll motions in beam seas, these inertial forces can exceed normal operational forces by a significant proportion. Thus the safety of the cargo is critically dependent on accurate predictions of motions of the barge induced by waves. This paper forms part of a study aimed at improving such predictions.

It is well known that the wave excitation and motions of certain large structures in gravity waves can be accurately estimated by the use of potential-flow theory. For such structures, viscous effects and the resultant skin-friction and pressure-drag forces are neglected. The validity of the potential-flow method is, however, limited by the extent to which smooth unseparated flow is maintained around the body in question. In particular, if a sharp edge induces local flow separation and consequent vorticity, the forces due to this viscous phenomenon are sufficient to affect the accuracy of the potential flow force and motion predictions.

This paper describes an experimental programme and complementary numerical results, which are compared to test the validity of the potential-flow theory for a shallow-draught flat-bottomed barge in waves. The numerical results are obtained by a boundary-integral approximate technique, which with the governing equations

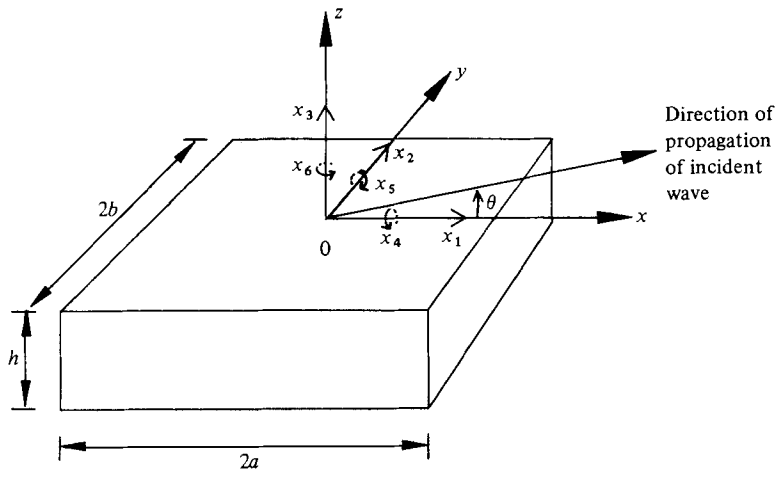

FIGURE 1. Definition of submerged geometry and axes.

of motion is briefly summarized in §2. Particular emphasis is placed on exploitation of symmetry of the barge, to achieve accurate numerical results economically. For the experimental investigation a notional prototype rectangular flat-bottomed barge of 86.40 m length, 28.80 m beam and 3.78 m draught is adopted. Data are acquired for two model scales, 1:36 and 1:108, thereby enabling some deductions to be made regarding the influence of scale effects on measured motions. Discrepancies between roll-motion results from the potential-flow theory and from the experiments in beam seas are discussed in some detail.

2. The theoretical model

2.1. *Equations of motion*

The theoretical predictions of barge motions are based on the assumptions of small responses in an inviscid fluid. The rigid body motions are designated ξ_j ($j = 1, \ldots, 6$), corresponding to surge, sway, heave, roll, pitch and yaw respectively. These are measured relative to a fixed set of axes located at the mean position of the centre of water plane area, with Ox in the plane of symmetry along the barge length and Oz directed positive upwards, as shown in figure 1. Since the motions are assumed to be small, it is unnecessary to distinguish between a body coordinate system and inertial axes fixed in space.

The barge is assumed to float in equilibrium with its centre of mass on the axis Oz. The equations of motion may be written in the matrix form

$$\boldsymbol{M}\ddot{\boldsymbol{\xi}} = \boldsymbol{X}, \tag{1}$$

where $\boldsymbol{X}$ is the column matrix of hydrodynamic forces and moments and

$$\boldsymbol{\xi} = \{\xi_1\ \xi_2\ \xi_3\ \xi_4\ \xi_5\ \xi_6\}. \tag{2}$$

Because of the symmetry in geometry and mass distribution of the barge, the inertia matrix $\boldsymbol{M}$ is diagonal except for the terms coupling surge with pitch and sway with roll ($M_{15}, M_{51}, M_{24}, M_{42}$).

The hydrodynamic loads are obtained by integrating the fluid pressures $p(x, y, z, t)$ over the submerged surface S_B of the barge. Thus for the force components

$$X_j = \int_{S_B} p n_j \mathrm{d}S \quad (j = 1, \ldots, 3), \tag{3}$$

where n_j are components of the unit normal $\boldsymbol{n}$ into the barge (in this case having the values ± 1). The hydrodynamic moment components are

$$X_j = \int_{S_B} p(\boldsymbol{r} \times \boldsymbol{n})_{j-3} \mathrm{d}S \quad (j = 4, 5, 6), \tag{4}$$

where $\boldsymbol{r}$ is the position vector (x, y, z).

2.2. *Numerical determination of hydrodynamic loads*

To obtain the fluid pressures one can invoke the assumptions of incompressible irrotational flow. The derivation is standard (see e.g. Newman 1977), but is briefly reviewed here in order to provide a basis for discussion of the numerical procedure adopted in the calculation of $\boldsymbol{X}$. Thus the fluid motions are described in terms of a velocity potential $\boldsymbol{\Phi}(x, y, z, t)$ such that the fluid velocity is $\nabla\boldsymbol{\Phi}$. From the linearized Bernoulli equation, the pressure in a fluid of density ρ is

$$p = -\rho \frac{\partial \boldsymbol{\Phi}}{\partial t} - \rho g z. \tag{5}$$

Hence the hydrodynamic loads may be obtained by substitution of (5) into (3) and (4). For a consistent linear theory this requires that the second component of p (resulting from the vertical pressure gradient) be integrated over the submerged volume in the displaced configuration, leading to components of the conventional hydrostatic restoring forces.

It is convenient first to examine loading by an incident sinusoidal wave of frequency ω. The response of the system, assumed linear, is then harmonic in time. We write

$$\boldsymbol{X} = \mathrm{Re}\,(\bar{\boldsymbol{X}} \mathrm{e}^{\mathrm{i}\omega t}), \tag{6a}$$

$$\boldsymbol{\xi} = \mathrm{Re}\,(\bar{\boldsymbol{\xi}} \mathrm{e}^{\mathrm{i}\omega t}), \tag{6b}$$

$$\boldsymbol{\Phi} = \mathrm{Re}\,(\boldsymbol{\phi}\, \mathrm{e}^{\mathrm{i}\omega t}). \tag{6c}$$

In the usual manner the spatial potential ϕ may be decomposed into

$$\phi = \phi_I + \phi_D + \mathrm{i}\omega \sum_{j=1}^{6} \bar{\xi}_j \phi_j, \tag{7}$$

where ϕ_I is the known potential of the incident wave and ϕ_D is the diffraction potential corresponding to scattering of the incident wave by the restrained barge. The radiation potentials ϕ_j are associated with unit motions of the barge in each of its six rigid-body modes in the absence of incident waves. These potentials satisfy the linearized free-surface boundary condition and the condition that there is no flow through the seabed. ϕ_D and ϕ_j satisfy the radiation condition for three-dimensional waves at infinity, and conditions ensuring that there is no flow through the submerged surface S_B.

The complex hydrodynamic loads $\bar{\boldsymbol{X}}$ are obtained by substituting (5)–(7) into (3) and (4), leading to the following matrix form:

$$\bar{\boldsymbol{X}} = -[-\omega^2 \boldsymbol{A} + \mathrm{i}\omega \boldsymbol{B} + \boldsymbol{C}]\,\bar{\boldsymbol{\xi}} + \bar{\boldsymbol{F}}. \tag{8}$$

Here the matrices $\boldsymbol{A}$, $\boldsymbol{B}$ and $\boldsymbol{C}$ correspond to added-mass, damping and hydrostatic

stiffness respectively, and $\bar{F}$ represents the wave excitation. In terms of the spatial potentials of (7) one finds

$$\bar{F}_j = -\mathrm{i}\omega\rho \int_{S_B} (\phi_I + \phi_D) \frac{\partial \phi_j}{\partial n} \mathrm{d}S, \tag{9a}$$

$$A_{jk} - \mathrm{i}\omega^{-1} B_{jk} = \rho \int_{S_B} \phi_k \frac{\partial \phi_j}{\partial n} \mathrm{d}S. \tag{9b}$$

Owing to the symmetry of the barge, the matrices $\boldsymbol{A}$ and $\boldsymbol{B}$ only contain terms on the diagonal and terms coupling surge with pitch and sway with roll. The only terms in $\boldsymbol{C}$ are the diagonal terms associated with heave, pitch and roll.

To obtain the motion responses of the barge, using (1), one must therefore first evaluate the diffraction and radiation potentials ϕ_D and ϕ_j. Even for the simple geometry under investigation here, it is necessary to use a numerical technique. Both boundary-element and finite-element methods have been applied to the hydrodynamic problem for a general three-dimensional body (as reviewed by Mei 1978; Eatock Taylor 1982). Either of these techniques could be used here, and the more recently developed coupled-element procedure has also been applied to an investigation of barge-type geometries (Eatock Taylor & Zietsman 1981).

The results presented below have been obtained from a conventional boundary-element implementation by use of a computer program called HYDRA, the background to which has been described by Eatock Taylor & Waite (1978). It uses distributed sources and sinks over the submerged surface of the body (the 'indirect' formulation), under the assumption of constant source over a flat quadrilateral panel. The following boundary-integral equations for the general case are used:

$$\phi(\boldsymbol{p}) = \frac{1}{4\pi} \int_{S_B} \sigma(\boldsymbol{q})\, G(\boldsymbol{p}; \boldsymbol{q})\, \mathrm{d}S, \tag{10a}$$

$$2\pi\, \sigma(\boldsymbol{p}) + \int_{S_B} \sigma(\boldsymbol{q}) \frac{\partial G(\boldsymbol{p}; \boldsymbol{q})}{\partial n_p} \mathrm{d}S = 4\pi \frac{\partial \phi(\boldsymbol{p})}{\partial n_p}, \tag{10b}$$

where $\phi(\boldsymbol{p})$ is the unknown potential at the point $\boldsymbol{p}$ on the submerged surface S_B and $\partial\phi(\boldsymbol{p})/\partial n_p$ is the given normal velocity, $v(\boldsymbol{p})$ say. The source strength at $\boldsymbol{p}$ is $\sigma(\boldsymbol{p})$, the associated normal into the surface is n_p, and the Green function is $G(\boldsymbol{p}; \boldsymbol{q})$. Equations (10$a$, b) are satisfied at a discrete number of points by a collocation technique, leading to the matrix equations

$$\boldsymbol{\phi} = \boldsymbol{P}\boldsymbol{\sigma}, \tag{11a}$$

$$\boldsymbol{Q}\boldsymbol{\sigma} = \boldsymbol{v}. \tag{11b}$$

Here the vectors $\boldsymbol{\phi}$, $\boldsymbol{\sigma}$ and $\boldsymbol{v}$ contain the potentials, source strengths and normal velocities at the collocation points, and the matrices $\boldsymbol{P}$ and $\boldsymbol{Q}$ are associated with integrals of the Green functions and their derivatives. Solution of (11b) for $\boldsymbol{\sigma}$, and substitution into (11a), yields the numerical approximation to the potentials on the surface S_B. Except near 'irregular' frequencies, discussed below, close approximations to the solutions of the boundary-value problems may be obtained with an appropriate choice of panels to idealize the submerged surface. From the vectors $\boldsymbol{\phi}$, approximations may readily be obtained to the added-mass and damping matrices and the wave forces.

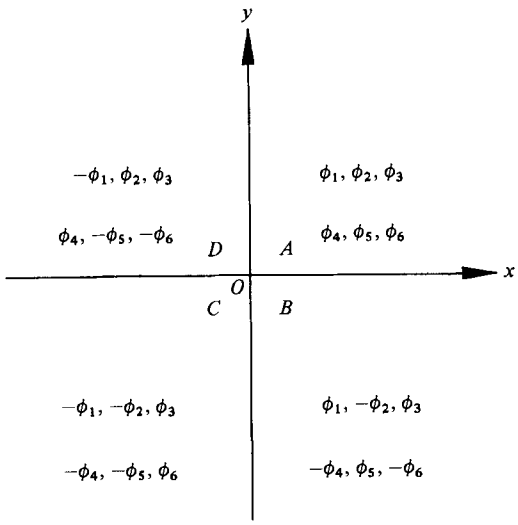

FIGURE 2. Specification of symmetries in the velocity potentials.

2.3. *Numerical features*

It is appropriate here to discuss the use of symmetry in the boundary-integral formulation. For a given computational resource (CPU memory or run time) this permits more accurate numerical results to be obtained than for an arbitrary body without planes of symmetry.

For a body such as the simple barge, the submerged surface S_B has two vertical planes of symmetry. The four quadrants of the semi-infinite fluid region defined by the planes Oxz, Oyz and the free surface are designated here as the regions A, B, C and D, according to the scheme shown in figure 2. The potentials, source strengths and normal velocities in region α ($\alpha = A, B, C, D$), are defined as $\boldsymbol{\phi}_\alpha$, $\boldsymbol{\sigma}_\alpha$, and $\boldsymbol{v}_\alpha$ respectively. The matrix $\boldsymbol{P}_{\alpha\beta}$ (cf. (11*a*)) is related to the Green functions coupling points in regions α and β ($\alpha, \beta = A, B, C, D$), with a corresponding definition for $\boldsymbol{Q}_{\alpha\beta}$. By consideration of symmetry it may readily be shown that $\boldsymbol{P}$ is of the form

$$\boldsymbol{P} = \begin{bmatrix} \boldsymbol{P}_{AA} & \boldsymbol{P}_{AB} & \boldsymbol{P}_{AC} & \boldsymbol{P}_{AD} \\ \boldsymbol{P}_{AB} & \boldsymbol{P}_{AA} & \boldsymbol{P}_{AD} & \boldsymbol{P}_{AC} \\ \boldsymbol{P}_{AC} & \boldsymbol{P}_{AD} & \boldsymbol{P}_{AA} & \boldsymbol{P}_{AB} \\ \boldsymbol{P}_{AD} & \boldsymbol{P}_{AC} & \boldsymbol{P}_{AB} & \boldsymbol{P}_{AA} \end{bmatrix},$$

and $\boldsymbol{Q}$ has similar symmetries.

To obtain $\boldsymbol{\phi}_\alpha$ in terms of the velocities $\boldsymbol{n}_\alpha$ it is useful to define the matrix

$$\boldsymbol{J} = \begin{bmatrix} \boldsymbol{I} & \boldsymbol{I} & \boldsymbol{I} & \boldsymbol{I} \\ \boldsymbol{I} & -\boldsymbol{I} & \boldsymbol{I} & -\boldsymbol{I} \\ \boldsymbol{I} & \boldsymbol{I} & -\boldsymbol{I} & -\boldsymbol{I} \\ \boldsymbol{I} & -\boldsymbol{I} & -\boldsymbol{I} & \boldsymbol{I} \end{bmatrix}, \tag{12}$$

where $\boldsymbol{I}$ is the identity matrix of order m (the number of collocation points in one quadrant). Premultiplication of (11*a*, *b*) by the matrix $\boldsymbol{J}$ then leads to the transformed equations

$$\boldsymbol{J}\boldsymbol{\phi} = \bar{\boldsymbol{P}}\bar{\boldsymbol{\sigma}}, \tag{13a}$$

$$\bar{\boldsymbol{Q}}\bar{\boldsymbol{\sigma}} = \boldsymbol{J}\boldsymbol{v}, \tag{13b}$$

where

$$\bar{\boldsymbol{\sigma}} = \boldsymbol{J}^{-1}\boldsymbol{\sigma}, \tag{14}$$

$$\bar{\boldsymbol{P}} = \boldsymbol{JPJ}, \tag{15a}$$

$$\bar{\boldsymbol{Q}} = \boldsymbol{JQJ}. \tag{15b}$$

The matrix $\bar{\boldsymbol{P}}$ is found to be of the form

$$\bar{\boldsymbol{P}} = 4\begin{bmatrix} \boldsymbol{P}_{AA}+\boldsymbol{P}_{AB}+\boldsymbol{P}_{AC}+\boldsymbol{P}_{AD} & 0 & 0 & 0 \\ 0 & \boldsymbol{P}_{AA}-\boldsymbol{P}_{AB}+\boldsymbol{P}_{AC}-\boldsymbol{P}_{AD} & 0 & 0 \\ 0 & 0 & \boldsymbol{P}_{AA}+\boldsymbol{P}_{AB}-\boldsymbol{P}_{AC}-\boldsymbol{P}_{AD} & 0 \\ 0 & 0 & 0 & \boldsymbol{P}_{AA}-\boldsymbol{P}_{AB}-\boldsymbol{P}_{AC}+\boldsymbol{P}_{AD} \end{bmatrix}$$

and $\bar{\boldsymbol{Q}}$ is similar. Hence (13b) may be solved for $\bar{\boldsymbol{\sigma}}$ by solving 4 systems of m equations, rather than one system of $4m$ equations required in the direct solution of (11b). Substitution of the solution into (13a) leads to

$$\boldsymbol{\phi} = \boldsymbol{J}^{-1}\bar{\boldsymbol{P}}\,\bar{\boldsymbol{Q}}^{-1}\boldsymbol{Jv}. \tag{16}$$

Noting that

$$\boldsymbol{J}^{-1} = \tfrac{1}{4}\boldsymbol{J}, \tag{17}$$

and defining the matrix

$$\bar{\boldsymbol{P}}\bar{\boldsymbol{Q}}^{-1} = \boldsymbol{S} = \begin{bmatrix} \boldsymbol{S}_1 & 0 & 0 & 0 \\ 0 & \boldsymbol{S}_2 & 0 & 0 \\ 0 & 0 & \boldsymbol{S}_3 & 0 \\ 0 & 0 & 0 & \boldsymbol{S}_4 \end{bmatrix}, \tag{18}$$

one finds that (16) may be written

$$\begin{bmatrix} \boldsymbol{\phi}_A \\ \boldsymbol{\phi}_B \\ \boldsymbol{\phi}_C \\ \boldsymbol{\phi}_D \end{bmatrix} = \frac{1}{4}\begin{bmatrix} \boldsymbol{\Sigma}_1 & \boldsymbol{\Sigma}_2 & \boldsymbol{\Sigma}_3 & \boldsymbol{\Sigma}_4 \\ \boldsymbol{\Sigma}_2 & \boldsymbol{\Sigma}_1 & \boldsymbol{\Sigma}_4 & \boldsymbol{\Sigma}_3 \\ \boldsymbol{\Sigma}_3 & \boldsymbol{\Sigma}_4 & \boldsymbol{\Sigma}_1 & \boldsymbol{\Sigma}_2 \\ \boldsymbol{\Sigma}_4 & \boldsymbol{\Sigma}_3 & \boldsymbol{\Sigma}_2 & \boldsymbol{\Sigma}_1 \end{bmatrix}\begin{bmatrix} \boldsymbol{v}_A \\ \boldsymbol{v}_B \\ \boldsymbol{v}_C \\ \boldsymbol{v}_D \end{bmatrix}, \tag{19}$$

where

$$\left.\begin{aligned} \boldsymbol{\Sigma}_1 &= \boldsymbol{S}_1+\boldsymbol{S}_2+\boldsymbol{S}_3+\boldsymbol{S}_4, \\ \boldsymbol{\Sigma}_2 &= \boldsymbol{S}_1-\boldsymbol{S}_2+\boldsymbol{S}_3-\boldsymbol{S}_4, \\ \boldsymbol{\Sigma}_3 &= \boldsymbol{S}_1+\boldsymbol{S}_2-\boldsymbol{S}_3-\boldsymbol{S}_4, \\ \boldsymbol{\Sigma}_4 &= \boldsymbol{S}_1-\boldsymbol{S}_2-\boldsymbol{S}_3+\boldsymbol{S}_4. \end{aligned}\right\} \tag{20}$$

The six radiation potentials are first considered, having the symmetries displayed in figure 2. Equation (19) shows that these potentials $\boldsymbol{\phi}$ have the same symmetries as the velocities $\boldsymbol{v}$. There are four independent cases, since surge [1] has the same symmetries as pitch [5], and sway [2] has the same as roll [4]. These cases are designated as follows: p for heave [3]; q for yaw [6]; r for surge/pitch [1, 5]; s for sway/roll [2, 4]. Then insertion of the appropriate symmetries into $\boldsymbol{v}$ in (19) yields

$$\left.\begin{aligned} \boldsymbol{\phi}_A^{\mathrm{p}} &= \boldsymbol{S}_1\boldsymbol{v}_A^{\mathrm{p}}, \quad \boldsymbol{\phi}_A^{\mathrm{q}} = \boldsymbol{S}_2\boldsymbol{v}_A^{\mathrm{q}}, \\ \boldsymbol{\phi}_A^{\mathrm{r}} &= \boldsymbol{S}_3\boldsymbol{v}_A^{\mathrm{r}}, \quad \boldsymbol{\phi}_A^{\mathrm{s}} = \boldsymbol{S}_4\boldsymbol{v}_A^{\mathrm{s}}. \end{aligned}\right\} \tag{21}$$

These are the vectors required in the evaluation of the added-mass and damping matrices, (9b), and it is evident that exploitation of the two planes of symmetry leads to a considerable reduction in the computation. It is only necessary to evaluate and

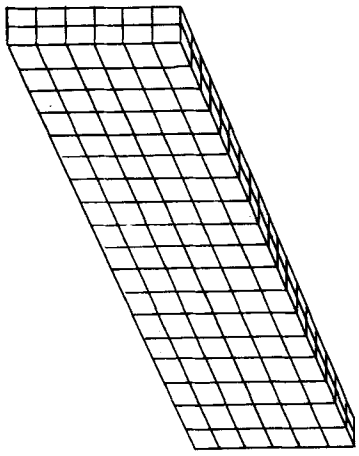

FIGURE 3. Mesh of one quadrant of barge submerged surface (viewed from below).

integrate the radiation potentials over one quadrant, and hence to solve four sets of equations of order m.

Computation of the wave forces on a body with two planes of symmetry cannot be reduced to quite the same extent. Only when the wave is propagating in the direction of a plane of symmetry do the incident and scattered wave potentials display symmetry or antisymmetry in their real or imaginary parts. They may, however, be written as the sum of symmetric and antisymmetric components. Use of (19) still incorporates major economies, since again it is only necessary to solve the four sets of equations of order m. If then the right-hand sides for the radiation problems are combined with the right-hand sides for the diffraction problems, the following equations of order m must be solved: two with two right-hand sides (using $\boldsymbol{S}_1$ and $\boldsymbol{S}_2$), and two with three right-hand sides (using $\boldsymbol{S}_3$ and $\boldsymbol{S}_4$). If symmetry were not exploited, one would need to solve one set of equations of order $4m$ (involving a fully populated coefficient matrix), with seven right-hand sides. This saving complements that associated with reducing by a factor of four the number of terms required for the matrices $\boldsymbol{P}$ and $\boldsymbol{Q}$ of (11).

In the calculations for the barge, collocation points were employed over one quadrant of the submerged surface. Each point was at the centre of a rectangular panel, the aspect ratio of which was in the range 1–1.34. The mesh covering one quadrant is shown in figure 3. Previous experience has shown that such a discretization is capable of yielding accurate results for potential-flow problems whose analytical solutions are known (e.g. circular cylinders). The major possible source of uncertainty regarding the numerical method arises from the phenomenon of 'irregular' frequencies discussed by John (1950) and more recently by Ursell (1981). These frequencies are associated with integral equations of the type given in (10), and they may be predicted analytically for certain geometries. This problem is briefly reviewed in the appendix, where an equation is given for the irregular frequencies corresponding to the rectangular barge. The theoretical motion responses for the two models considered herein are evaluated within a frequency range sufficiently below the lowest irregular frequency that no numerical difficulty would arise from this source.

2.4. *Motion response to random waves*

The experimental results presented in §3 were obtained by measuring responses of the barge in long-crested random waves. The plotted data comprise transfer functions

(response amplitude operators) corresponding to responses of the barge in unit-amplitude sinusoidal waves. The theoretical and experimental transfer functions for the motion responses were obtained as follows.

Substitution of (8) and (6) into (1) leads to

$$[-\omega^2(\boldsymbol{M}+\boldsymbol{A})+\mathrm{i}\omega\boldsymbol{B}+\boldsymbol{C}]\bar{\boldsymbol{\xi}}=\bar{\boldsymbol{F}}. \tag{22}$$

One may thus obtain the theoretical responses in waves of amplitude $\bar{\zeta}$ at frequency ω in direction θ to Ox as

$$\bar{\boldsymbol{\xi}}(\omega,\theta)=\boldsymbol{H}_{f\xi}(\omega)\bar{\boldsymbol{f}}(\omega,\theta)\,\bar{\zeta}, \tag{23}$$

where the receptance matrix is

$$\boldsymbol{H}_{f\xi}=[-\omega^2(\boldsymbol{M}+\boldsymbol{A})+\mathrm{i}\omega\boldsymbol{B}+\boldsymbol{C}]^{-1}, \tag{24}$$

and the wave loads are given by

$$\bar{\boldsymbol{F}}=\bar{\boldsymbol{f}}(\omega,\theta)\,\bar{\zeta}. \tag{25}$$

One can thus define the column matrix of response amplitude operators as

$$\boldsymbol{H}_{\zeta\xi}(\omega,\theta)=\boldsymbol{H}_{f\xi}(\omega)\bar{\boldsymbol{f}}(\omega,\theta). \tag{26}$$

In (26) the numerical solution for the diffraction potential is incorporated in $\bar{\boldsymbol{f}}(\omega,\theta)$, whereas the terms of $\boldsymbol{H}_{f\xi}(\omega)$ are obtained using the radiation potentials (use of the well-known relationships between radiation and diffraction potentials (e.g. Newman 1977) would be possible, but does not yield any significant advantage in the present context).

Equations (23) and (26) provide the basis for extracting the barge response amplitude operators in random waves. For a long-crested sea having a one-sided wave elevation spectrum $S_{\zeta\zeta}(\omega)$, the column matrix of cross-spectra between wave and response is

$$\boldsymbol{S}_{\zeta\xi}(\omega,\theta)=S_{\zeta\zeta}(\omega)\,\boldsymbol{H}_{\zeta\xi}(\omega,\theta). \tag{27}$$

The direct response spectra are given by

$$S_{\xi_j\xi_j}(\omega,\theta)=|H_{\zeta\xi_j}(\omega,\theta)|^2\,S_{\zeta\zeta}(\omega)\quad(j=1,\ldots,6). \tag{28}$$

In the experiments described below, responses $\xi(t,\theta)$ to random waves $\zeta(t)$ are measured, and the direct and cross-spectra $\boldsymbol{S}_{\xi\xi}$, $\boldsymbol{S}_{\zeta\zeta}$ and $\boldsymbol{S}_{\zeta\xi}$ are estimated from the sampled data. From the second and third of these, the modulus and phase of the 'measured' transfer functions $H_{\zeta\xi_j}$ are evaluated by means of (27). The independent estimate of $|H_{\zeta\xi_j}|$, provided by (28), permits an assessment to be made of the reliability of the theoretical model and the measurement techniques, by examination of the resulting coherence functions (e.g. Bendat & Piersol 1971).

3. The experimental programme

3.1. *Small-scale model tests at University College London*

The small-scale tests were performed in a wave tank at the Department of Mechanical Engineering, University College London. The tank is 14.8 m long, 2.20 m wide, with 1 m water depth. It is fitted with a wedge-type electrohydraulically actuated wave generator capable of producing long-crested regular and random waves.

A 1:108 scale model of the prototype barge described in §1 was used in these tests. The model barge dimensions were 800 mm length, 267 mm beam, with a total height of 100 mm; the latter being chosen to be slightly greater than the value for 1:108

Physical property	Scale factor	1:36 scale values	1:108 scale values
Length/m	α	2.400	0.800
Beam/m	α	0.800	0.267
Height/m	α	0.340	0.100
Draught/m	α	0.105	0.0345
Radius of curvature of rounded keel edge/m	α	0.040	0.013
Mass/kg	α^3	200.8	7.375
Roll radius of gyration/m	α	0.244	0.080
Pitch radius of gyration/m	α	0.688	0.225
Yaw radius of gyration/m	α	0.598	—
Roll moment of inertia/kg m^2	α^5	11.95	0.047
Pitch moment of inertia/kg m^2	α^5	95.05	0.373
Yaw moment of inertia/kg m^2	α^5	71.81	—
Distance of centre of gravity above keel/m	α	0.111	0.035
Roll natural frequency/rad s^{-1}	$\alpha^{\frac{1}{2}}$	5.8	10.5

TABLE 1. Physical properties and scale factors for model barges

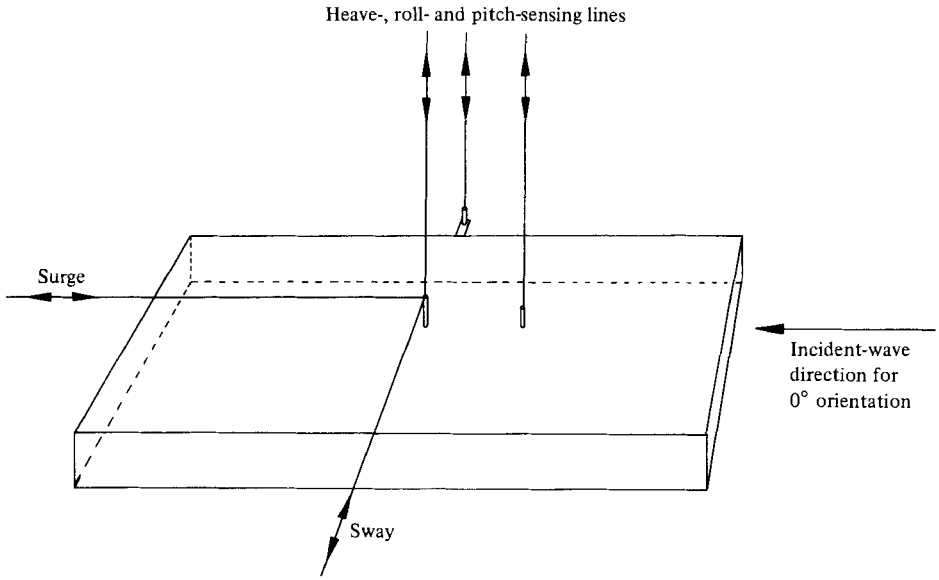

FIGURE 4. Motion-sensing lines on 1:108 scale barge model.

scale, to avoid deck-immersion effects during roll motions. The model was constructed with marine ply around a softwood frame. The structure was designed such that the bottom horizontal edges around the keel could be removed and refitted with either sharp or rounded keel-edges (the latter of 13 mm radius of curvature). The barge model was ballasted to a draught of 34.5 mm. Table 1 gives a list of the physical properties of the model barge, associated with Froude-number scaling. It should be noted that the model barge masses, radii of gyration, moments of inertia and roll natural frequencies given in table 1 were obtained by measurements on the models rather than direct application of the scaling rules.

The barge model motions in waves were measured by five conductive plastic high-resolution low-friction rotary potentiometers mounted with pulleys. Light nylon

lines were run over the pulleys to pillars on the model deck, the lines being kept taut by small weights at their free ends.

As shown in figure 4, three of these lines were vertical and were used to detect barge heave, roll and pitch motions. The latter were extracted from the differential motions of the lines in the corresponding vertical planes. The two horizontal lines were used to sense surge and sway motions. The yaw degree of freedom was not recorded in these tests. The potentiometers were excited by a d.c. voltage, the central wipers providing an electrical output proportional to potentiometer-pulley angular displacement. The directions of the measured motion outputs were defined by the system of axes shown in figure 1.

The potentiometer outputs were recorded by a computer-controlled data-sampling system. A short preprocessor computer program used the raw potentiometer outputs to extract roll and pitch motions, to correct for interaction effects between the motions, and to convert the measured horizontal motions to surge and pitch motions of the barge centroid.

Barge tests in waves were preceded by static tests to ensure that the model floated on an even keel, and to measure the position of centre of gravity. Its radii of gyration about the roll and pitch axes through the centre of gravity were also measured. These data are presented in table 1.

Since the barge model significantly influences its local wave environment, owing to wave diffraction and radiation, measurements of the incident wave were made by removing the model and placing an a.c. reactance-sensing twin-wire wave probe at the position of the barge vertical centreline. The resultant records of incident wavetrains were matched with the subsequent tests for the barge in waves by means of an accurate reference timing signal. This was generated by the microprocessor that controlled the wavemaker, and enabled the data logger to be triggered into operation at a precisely defined point in the incident-wave time history.

For the wave tests, the barge was moored by a four-point system of slack, very elastic lines connecting its corners to the tank sides. The lines remained slack and floated horizontally on the water surface during normal testing.

Both regular and random wave tests were conducted. The regular wave tests were run with 0° (head seas) and 90° (beam seas) wave orientations for a frequency range of 0.5–1.9 Hz spanning the roll and pitch resonant motions of the vessel with wave amplitudes of 1 and 1.5 cm. A data-sampling rate of 25 Hz was used for a period of 8 s to yield 200 points per channel. Measurements were made with both rounded and sharp keel-edge profiles fitted. The random-wave data were also obtained for the barge in head and beam seas. A Pierson Moskowitz incident-wave elevation spectrum was used with three significant wave heights of 1, 2 and 3 cm and characteristic periods of 0.7, 0.9 and 1.3 s. The control signals driving the electrohydraulic wavemaker were calculated in real time by digitally filtering a pseudo-random shift-register sequence. Figure 6(*a*) shows the measured spectra for a significant wave height of 3 cm. All the wave and barge-response data were recorded for 250 s at a 10 Hz sampling rate to give 2500 data points per measured channel. These data were stored directly on a computer disc. Section 3.3 describes the processing of this raw data in further detail.

3.2. *Large-scale model tests at the Hydraulics Research Station*

These tests were conducted in a complex sea basin at the Hydraulics Research Station, Wallingford. The basin is 18 m square, with a water depth of 1.5 m. Waves are produced by 10 independent wedge-type paddles situated along one side of the basin, with wave-absorbing beaches mounted on the other three sides. For these

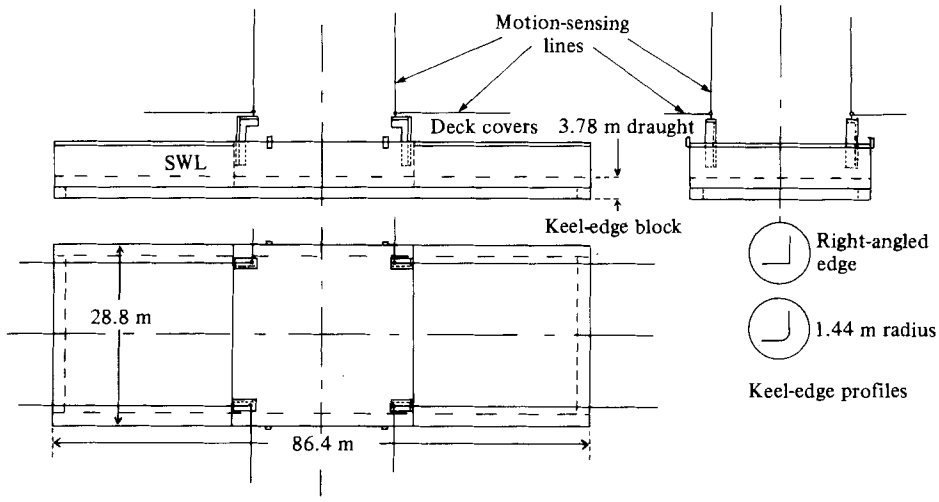

FIGURE 5. The 1:36 scale-model barge structure. Note that dimensions given correspond to the full-scale barge.

experiments, each of the 10 electrohydraulically actuated paddles was driven by an identical signal from a central control unit, thereby generating long-crested waves. Control signals for regular wave tests were generated by an analogue oscillator. Random waves were produced in the manner described for the U.C.L. tests in §3.1.

The model used in these tests (shown in figure 5) was a 1:36 Froude-number-scaled replica of the prototype barge. It was of 2.400 m length, 0.800 m beam, and used with 0.105 m draught. The total barge height of 0.240 m was again slightly higher than the true scale value to avoid deck immersion at large roll angles. The barge model was constructed out of 12.7 mm thick marine ply with a 25 mm square softwood frame. The structure was designed to allow the mounting of 47 mm square keel-edge blocks around the submerged horizontal edges of the barge. Two choices of keel-edge profiles were again available: a right-angled 'sharp' edge and a rounded profile of 40 mm radius of curvature. Characteristics of the model, including measured position of the centre of gravity and moments of inertia, are listed in table 1.

Motions of the test barge in all six degrees of freedom (surge, sway, heave, roll, pitch and yaw) were measured by a system of 12 nylon lines connecting the barge to potentiometers above and on the sides of the wave basin. Three nylon lines were run from each of four points on the structure (see figure 5) in a manner similar to that already described. An analogue signal conditioning system was used to correct the raw analogue data for interactions between the modes of motion.

As with the 1:108 scale tests, the incident waves were measured, with the barge removed from the basin, at the vertical centreline position of the barge. The wave data were recorded, together with a sinusoidal timing signal which enabled the wave and subsequent motion data to be matched.

A spread mooring system was used from four points on the barge. During normal testing the mooring lines remained slack and floating on the water surface. Excessive wave drift was prevented by the mooring lines acting as a hardening spring as they lifted out of the water and became taut. No measurements were recorded during such occurrences.

Measurements of barge motions in waves were made for both regular and random

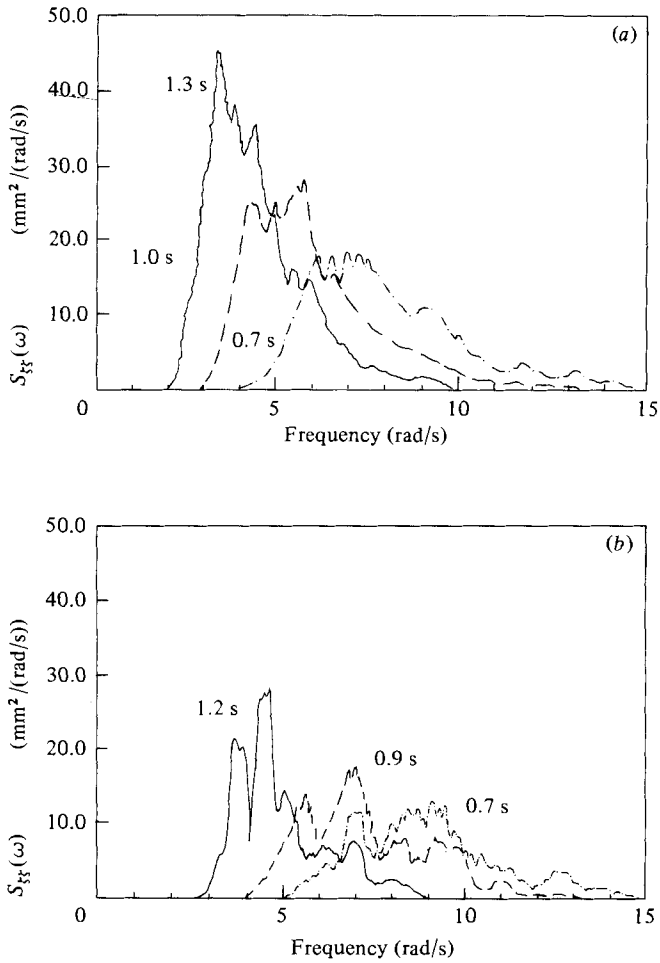

FIGURE 6. Wave-elevation power-spectral densities. (*a*) 1:108 scale tests; (*b*) 1:36 scale tests. 3 cm significant wave height, 0.7, 1.0 and 1.3 s characteristic periods.

waves of three orientations: 0° (head seas), 45° (quartering seas) and 90° (beam seas) for both sharp and rounded keel-edge profiles. Regular wave data were taken for three wave heights of between 1 and 3 cm over a frequency range from 0.5 to 1.60 Hz. Data were sampled for 8 s at a sampling rate of 16 Hz. The random wave tests were conducted with nine Pierson Moskowitz wave spectra at three significant wave heights in the range from 1.8 to 5.4 cm and three characteristic periods (0.7, 0.9 and 1.3 s). Figure 6(*b*) shows three such spectra for a significant wave height of 3.0 cm. The random wave data were sampled at a rate of 16 Hz for a period of 256 s giving 4096 data points per measured channel. A total of nine such channels were recorded: a wave-elevation and timing-signal channel for the wave measurement; and the six motion channels plus the timing-signal channel again for the motion measurements. The data were recorded on magnetic tape.

3.3. *Data analysis*

The data collected from the 1:108 scale wave and corresponding barge-motion experiments were already correctly timed: both corresponding runs had been sampled

starting from a common trigger signal. For the 1:36 scale tests, however, the random wave and barge-motion data were matched by a simple computer program. This identified specific features in the timing signal channels and matched up the wave and motion measurements data appropriately. Slight variations in the driving clock frequencies for the wave-generator control signals required the response data to be slightly stretched and modified by a cubic-spline interpolation technique. Core records of 3840 data points were obtained after these matching operations.

For both 1:36 and 1:108 scale tests, the regular wave data were first analysed by a routine which searched for peaks and troughs in order to determine the frequency of the incident regular wave. This frequency was then used in a simple numerical harmonic analysis, which computed the amplitudes and phases of each response relative to the wave. These regular wave data were invariably found to be in accordance with the random wave transfer functions presented in figures 6–18 inclusive, and they are therefore not presented in further detail herein.

Spectral estimates of the random wave and response data were obtained by performing fast-Fourier-transform (FFT) operations directly on the time-series data. The accuracy of the spectral estimates was improved by first obtaining a zero mean of each sampled channel, then multiplying by a one-tenth cosine-tapered data window and finally packing out the channel with zeros to make a total of 4096 data points. The resulting spectral estimates were multiplied by appropriate factors to correct for the distortions introduced by these last two steps.

The fast-Fourier-transform operations yielded 2049 raw auto- and cross-spectral estimates at frequency intervals of 0.0245436 rad/s starting from 0 rad/s. Final smoothed spectral estimates were obtained from a moving average of 21 adjacent raw estimates and every third of these was plotted to generate the data of figures 6–19. The transfer functions are only presented for a frequency range over which there is sufficient energy in the corresponding wave spectra, and were obtained from the cross-spectral estimates by means of (27). Over this frequency range the coherence remained high (> 0.8) except in small regions where nonlinear effects dominated.

4. The results

Only the head- and beam-sea data for the random wave tests are presented here. The sway, roll and yaw responses for head seas and the surge, pitch and yaw responses for beam seas remained negligibly small throughout the tests, as is to be expected. These responses are therefore not considered further.

The incident-wave spectra for both the 1:108 and 1:36 scale tests (figure 6) are not exceptional. The spectra obtained in the two wave tanks are somewhat different, although this is not expected to influence the transfer functions evaluated from the two facilities to any significant extent. The reasons for this behaviour are not clear. The fast-Fourier-transform routine is not the cause, since it was essentially identical for the analysis of both sets of test data.

The transfer functions for surge, sway, heave, pitch and roll from the tests at both scales are presented in figures 7–18. In all cases, full and dashed lines denote the transfer functions obtained from the rounded and sharp keel-edge profiles respectively. The asterisks denote theoretical results based on the analysis of §2. The experimental transfer functions obtained from different values of significant wave height or regular wave heights are measured to be identical within the bounds of experimental error. No discernible effects of wave-amplitude-dependent nonlinearity were observed, even for the data at and roll resonance. The feature is illustrated by

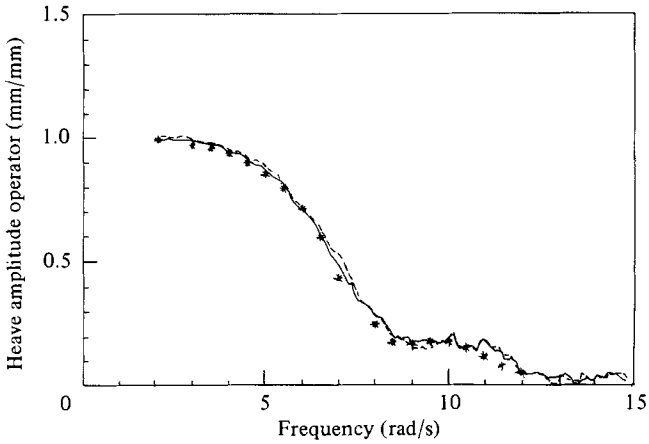

FIGURE 7. Heave transfer function in head seas for 1:108 scale; full and dotted lines denote data for rounded and sharp keel-edge profiles respectively; asterisks denote theory.

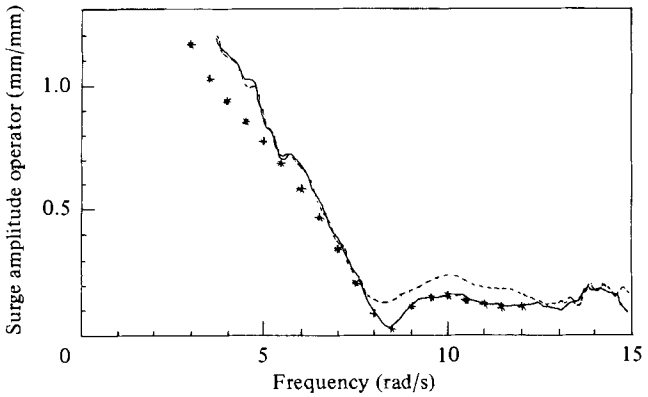

FIGURE 8. Surge transfer function in head seas for 1:108 scale; full and dotted lines denote data for rounded and sharp keel-edge profiles respectively; asterisks denote theory.

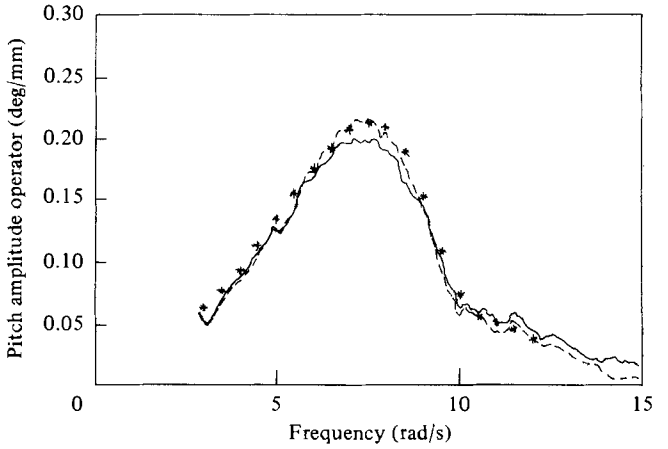

FIGURE 9. Pitch transfer function in head seas for 1:108 scale; full and dotted lines denote data for rounded and sharp keel-edge profiles respectively; asterisks denote theory.

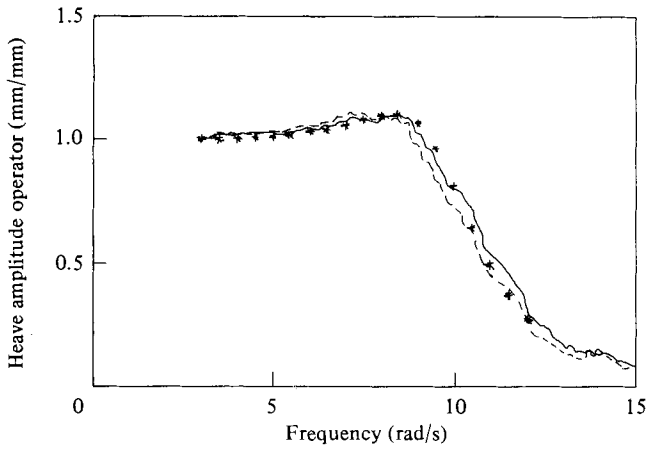

FIGURE 10. Heave transfer function in beam seas for 1:108 scale; full and dotted lines denote data for rounded and sharp keel-edge profiles respectively; asterisks denote theory.

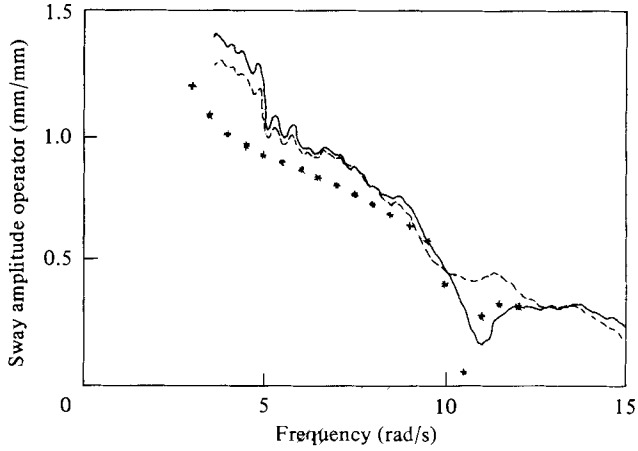

FIGURE 11. Sway transfer function in beam seas for 1:108 scale; full and dotted lines denote data for rounded and sharp keel-edge profiles respectively; asterisks denote theory.

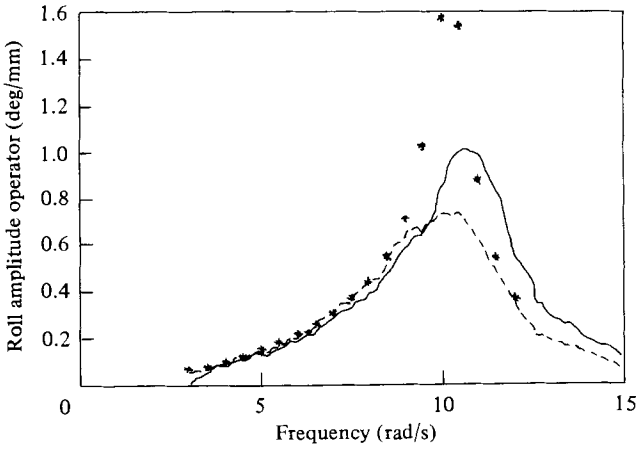

FIGURE 12. Roll transfer function in beam seas for 1:108 scale; full and dotted lines denote data for rounded and sharp keel-edge profiles respectively; asterisks denote theory.

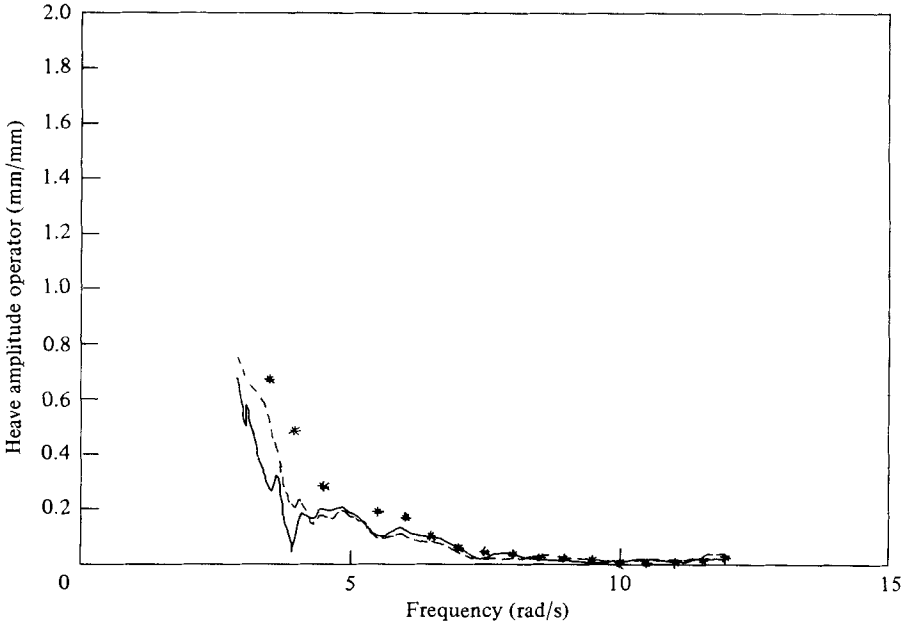

FIGURE 13. Heave transfer function in head seas for 1:36 scale; full and dotted lines denote data for rounded and sharp keel-edge profiles respectively; asterisks denote theory.

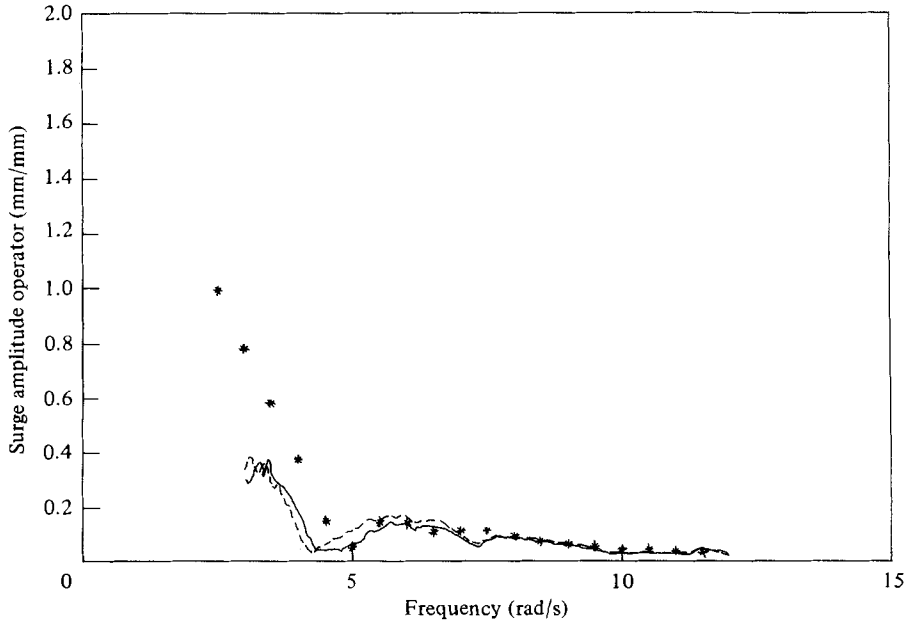

FIGURE 14. Surge transfer function in head seas for 1:36 scale; full and dotted lines denote data for rounded and sharp keel-edge profiles respectively; asterisks denote theory.

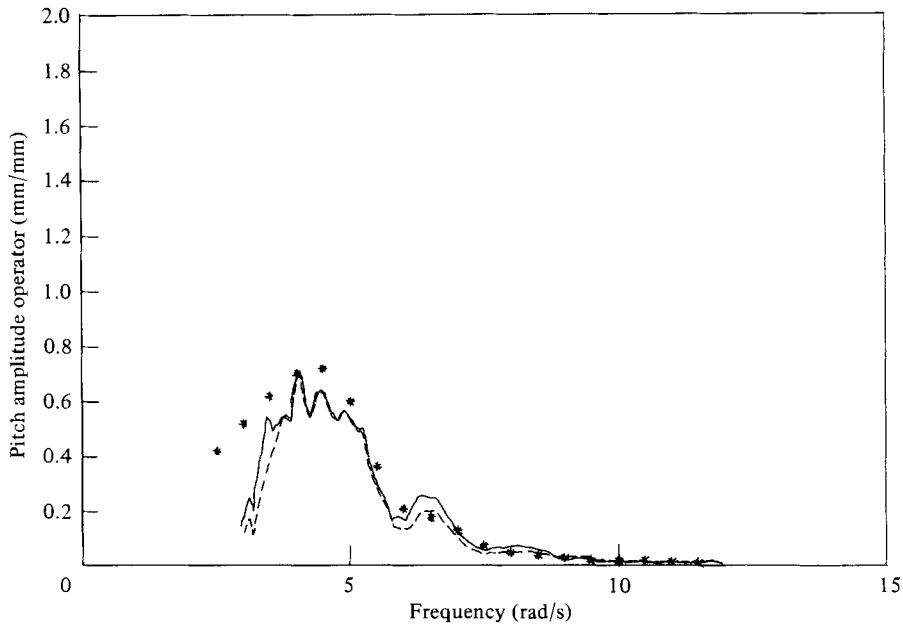

FIGURE 15. Pitch transfer function in head seas for 1:36 scale; full and dotted lines denote data for rounded and sharp keel-edge profiles respectively; asterisks denote theory.

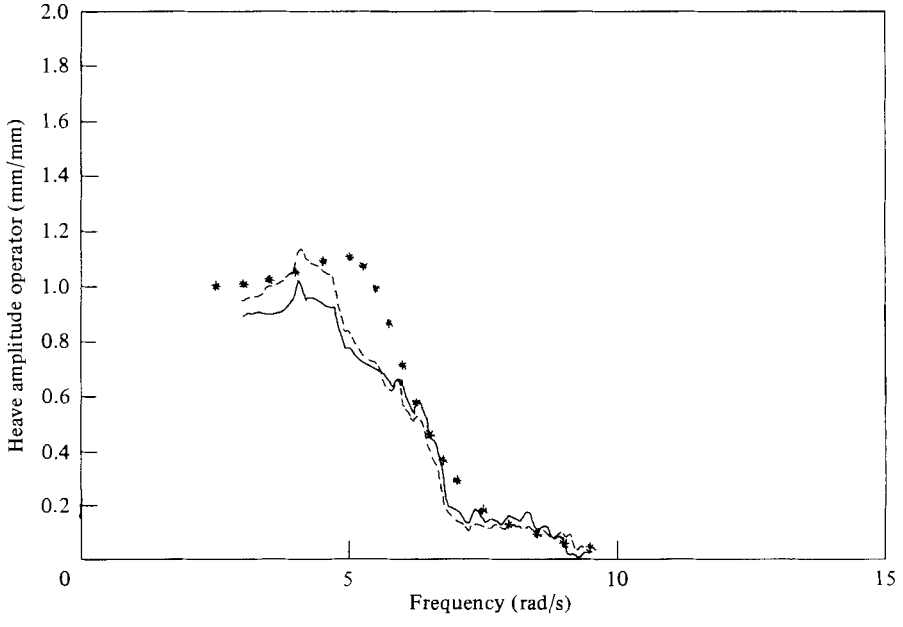

FIGURE 16. Heave transfer function in beam seas for 1:36 scale; full and dotted lines denote data for rounded and sharp keel-edge profiles respectively; asterisks denote theory.

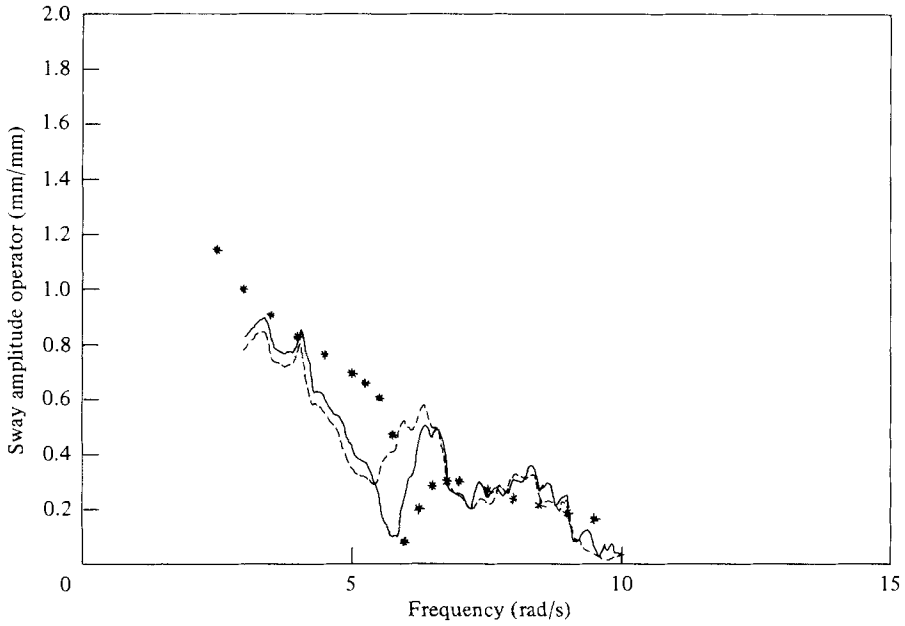

FIGURE 17. Sway transfer function in beam seas for 1:36 scale; full and dotted lines denote data for rounded and sharp keel-edge profiles respectively; asterisks denote theory.

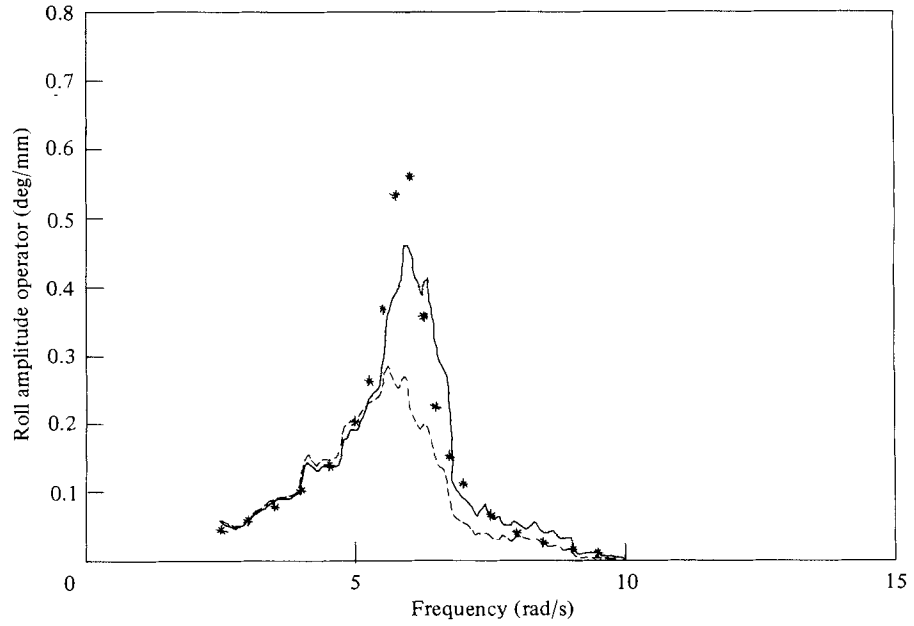

FIGURE 18. Roll transfer function in beam seas for 1:36 scale; full and dotted lines denote data for rounded and sharp keel-edge profiles respectively; asterisks denote theory.

figure 19, showing roll-motion data for the 1:36 scale barge in beam seas for three different significant incident wave heights. The error bar on the figure gives an estimate of the measurement error.

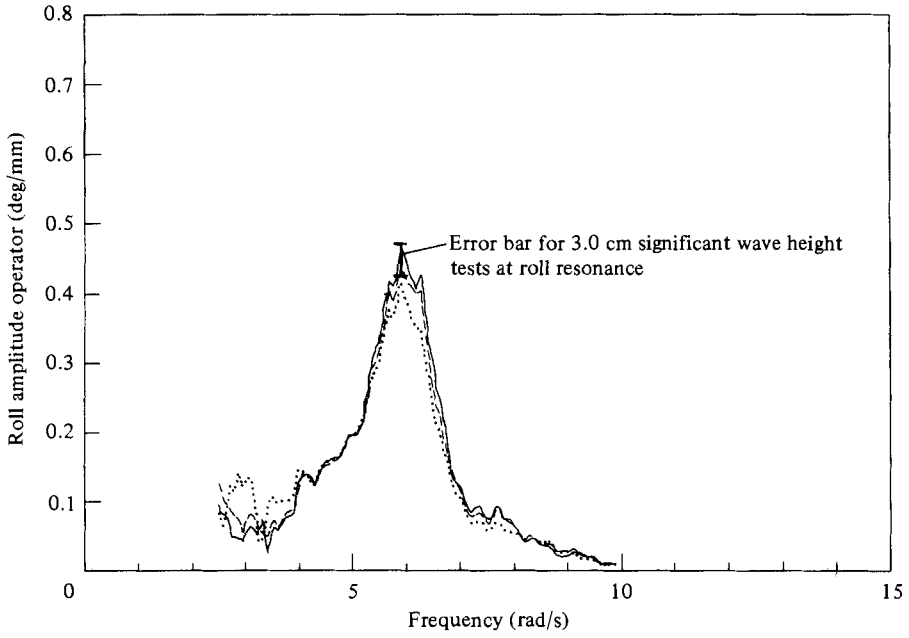

FIGURE 19. Roll transfer function in beam seas for 1:36 scale barge with rounded keel-edges; full, dashed and dotted lines denote data for significant wave heights of 3.0, 2.4 and 1.9 cm respectively.

4.1. *Head seas*

Figures 7 and 13 present the heave response to head seas for the 1:108 and 1:36 scale tests respectively. The transfer functions for sharp and rounded keel-edges are very close, and they both agree with the potential-flow theory. One evident feature of these figures is the larger discrepancy between theory and experiment for figure 13 than for figure 7. It is believed that this discrepancy in figure 13 and the generally poorer agreement between theory and experiment for the 1:36 scale results is partly related to the data-collection system in these tests. As described earlier, measurements were made by placing a wave probe at the barge position, sampling wave elevations and then sampling barge motions with the barge in the wave-probe position. The two measurements were matched by also measuring a channel of the wave-generator driving-clock signal. There was, however, a small drift in this clock rate between wave-elevation and barge-motion measurements. The drift was accommodated in the data processing by using interpolation techniques to match the wave-elevation and barge-motion time histories. Small errors of signal level in this procedure are felt to be responsible for the scatter in the 1:36 scale data and for the discrepancies between theory and experiment. It may be noted that the kind of clock-rate drift that occurred in 1:36 scale tests did not occur for the 1:108 scale tests.

Figures 8 and 14 give corresponding data for the surge response in head seas. It should first be noted that the measured surge-response time history for the 1:36 scale tests provided evidence of a low-frequency wave-drift oscillation at approximately 0.5 rad/s with a small root-mean-square value of approximately 4 mm. This does not, however, influence the data plotted in figure 14. The surge-response transfer function at wave frequencies indicates a difference between the sharp and rounded keel-edge profiles around the wave cancellation frequency of 8.4 rad/s for 1:108 scale and 4.8 rad/s for 1:36 scale: the sharp keel-edge for both models leading to higher

responses. A discrepancy between experiment and theory appears at low frequencies. There is sufficient energy at these low frequencies to discount numerical errors as a cause of this discrepancy, which occurs for tests at both scales. The probable explanation is the low-frequency partial standing wave that occurs in wave tanks of finite length caused by the reflections that arise from the wave-absorbing beach for these low frequencies. The partial standing wave forms a 'sloshing' component in the bulk of the wave-tank fluid and induces enhanced horizontal, oscillating, fluid velocities and accelerations in the centre of the tank at the test-model position. Furthermore, experience of testing in different types of tanks indicates that the effect of these low-frequency standing-wave components are more severe in tanks with approximately equal length and width than in long tanks of relatively small width. This is because the former type of tank has standing waves with variations in both the longitudinal and transverse directions, which are likely to affect the test model more severely.

Figures 9 and 15 present data for pitch responses in head seas. The data at both scales are very close, for both rounded and sharp keel-edges, to the results from potential-flow theory. There are no unusual features of the pitch response that can be identified with sufficient confidence.

4.2. *Beam seas*

Figures 10 and 16 display heave transfer functions for 1:108 and 1:36 scale tests respectively. The barge responses for both sharp- and rounded-edge cases are very close to each other and to the theory. Figures 11 and 17 present sway transfer functions in beam seas. This mode of motion (like surge in head seas) also exhibited low-frequency drift effects, which for the 1:36 scale tests were at approximately 0.5 rad/s with a root-mean-square intensity of 2.3 cm for the rounded keel-edges. The sway transfer functions for rounded and sharp keel-edges are very close except for a region around roll resonance where the sharp keel-edge data are substantially higher. Furthermore, both sets of experimental data differ from the potential-flow theory for the lower frequencies. This difference is in opposite senses for the 1:108 and 1:36 scale tests.

Figures 12, 18 and 19 present the roll motion transfer functions in beam seas. These data indicate substantial differences between the sharp and rounded keel-edge experimental data as well as between experiment and theory. The plotted roll responses are centred around the roll resonance frequency (10.5 rad/s for 1:108 scale and 5.8 rad/s for 1:36 scale). Roll motions for the rounded keel-edges are seen to be up to 50% greater than those for sharp edges near and above the roll resonance frequency.

During the beam-sea tests, there was a noticeable difference between the local water motions close to the barge in the cases of rounded and sharp keel-edges, the latter generating a large amount of turbulence in and under the free surface. Despite the relatively smoother flow observed close to the rounded keel-edges during the tests, experiment and theory for this case still disagree substantially at resonance, for tests at both scales. The relative extent of the discrepancy between the rounded and sharp edges is approximately the same for both scales. On the other hand the differences between theory and the rounded keel-edge data are discernibly larger for the 1:108 scale than for the 1:36 scale tests, suggesting that viscous effects are playing a relatively larger role at smaller scale. Both sets of roll response data also show a slight reduction in the roll natural frequency from rounded to sharp keel-edge data. This would be consistent with an increase in damping, due to vortex shedding and fluid turbulence induced by the sharp keel-edges.

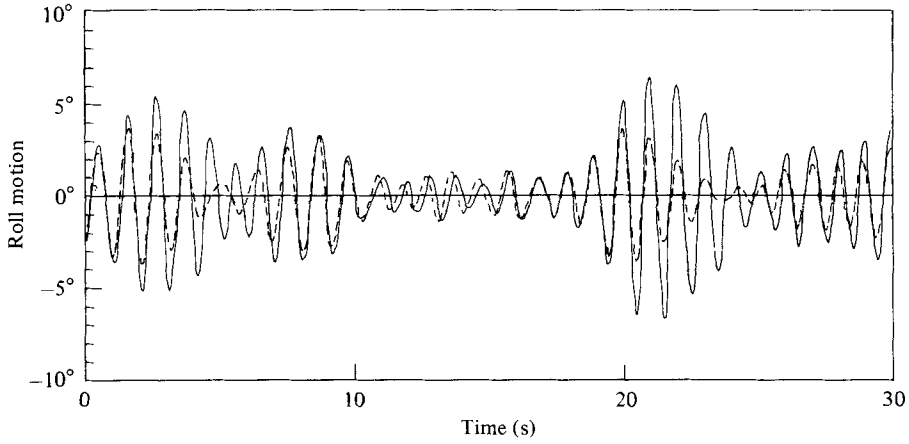

FIGURE 20. Comparison of roll-time history from 1:36 scale tests for two keel-edge profiles; full and dotted lines denote data for rounded and sharp keel-edge profiles respectively. Significant wave height = 3.4 cm; characteristic period = 0.9 s.

The differences between the rounded and sharp keel-edge experimental data are also brought out by the plots of roll angle against time displayed in figure 20 for the two conditions. Peak roll angles for the rounded keel-edges are approximately double those measured for the sharp keel-edges, thus illustrating the need for a sound theory to account for the viscous effects at the vessel keel, and more accurately to predict the roll motion responses of cargo-carrying barges. It is worth noting the manner in which the difference between the rounded and sharp keel-edge data develops with time. It suggests a vortex-shedding or turbulence-generation process, which is triggered off by roll motions reaching a particular amplitude. The discrepancy caused by these viscous effects persists for a while before decaying, and the triggering process is then repeated.

Additional work, not described here, has shown that the observed discrepancies in roll motion can be accommodated by increasing the potential-flow radiation damping by approximately 20% of critical damping for the rounded keel-edge and 80% of the same for the sharp keel-edge. Furthermore, visualization studies of the flow close to the keel-edge reveal the presence of strong vortex shedding and consequent vortex movements around the keel. Such vortex shedding is not detected for the rounded keel-edges. These studies suggest that the observed discrepancies in roll motions can be predicted by an analytical model which uses point vortices in a background potential flow together with skin-friction calculations to predict the energy dissipated and consequential additional damping due to these viscous effects. Patel & Brown (1981; and Brown & Patel 1981) give a description of methods used and some intermediate results.

5. Conclusions

An overview of the results presented here for the motion response to waves of flat-bottomed barges suggests that, for the incident-wave amplitudes used in the tests, the motion response is strongly linear with no suggestions of response variations as a function of wave amplitude. The validity of potential-flow theory for all motions except sway and roll in beam seas is confirmed, by comparisons of the theory with tests at two model scales. In the case of sway motions in beam seas, discrepancies

between theory and experiment at low frequencies cannot be easily explained, but may be due to excitation by a standing-wave motion component in both wave-tank facilities. Such an effect is also apparent for surge motions in head seas. Potential-flow theory is shown to be incapable of satisfactorily predicting roll motions at resonance for both rounded and sharp keel-edge profiles; the discrepancy for the latter being approximately twice as large as for the former. It is generally accepted that the discrepancy for the sharp keel-edge profiles is due to the added damping induced by vortex shedding and the generation of turbulence close to the keel-edges. Even for the rounded keel-edges, however, sufficient drag associated with skin friction exists to induce the observed discrepancies. Further research on these aspects of the problem has been discussed in §4.

The testing of an identical barge model shape at two different scales affords a unique opportunity to investigate the quantitative effects of model scale on measurements such as these. A survey of all the data presented here only reveals possible scale effects for the roll response in beam seas. This is to be expected, since it is the relative magnitude of inertia and viscous forces which leads to the occurrence of scale effects in model testing, and viscous effects only become significant at and around roll resonance during the experiments reported here.

The authors wish to acknowledge the support of this work by the Marine Technology Directorate of the Science and Engineering Research Council, U.K., under grant no. GR/B/21812. SERC support for use of the complex wave basin at the Hydraulics Research Station is also gratefully acknowledged. The authors wish to thank Dr P. E. Duncan, Mr P. C. Petrides and HRS staff for their contributions to the experimental work reported here.

Appendix. Irregular frequencies in the boundary-integral analysis

It is well known that Fredholm integral equations of the type given in (10), for time-harmonic exterior problems, do not have unique solutions at certain frequencies. John (1950) has given a formal discussion of this difficulty for water-wave diffraction and radiation, and Shaw (1979) has briefly reviewed recent attempts to overcome it in numerical solution of such integral equations for general wave problems.

In the numerical approach represented by (11), the matrices $\boldsymbol{P}$ and $\boldsymbol{Q}$ both become very badly conditioned near an irregular frequency. This is potentially serious unless one can predict such frequencies, which in the case of the barge is trivial. It may be shown generally that these occur at the eigenfrequencies of the corresponding interior Dirichlet problem for the potential. For the barge, therefore, of plan dimensions $2a \times 2b$ and draught h, eigenvalues are required for the problem defined by

$$\left.\begin{aligned} \nabla^2\bar{\phi} &= 0, \\ \frac{\partial\bar{\phi}}{\partial z} - \frac{\omega^2}{g}\bar{\phi} &= 0 \quad (z = 0), \\ \bar{\phi} &= 0 \quad (x = \pm a,\ y = \pm b,\ z = -h), \end{aligned}\right\} \tag{A 1}$$

where $\bar{\phi}$ is the potential interior to the submerged surface S_B. Direct solution of (A 1) leads to irregular frequencies ω_{mn}, which are the roots of

$$\kappa \coth \kappa h = \frac{\omega_{mn}^2}{g}, \tag{A 2}$$

where

$$\kappa^2 = \left(\frac{m\pi}{2a}\right)^2 + \left(\frac{n\pi}{2b}\right)^2 \quad (m, n = 1, 2, \ldots). \tag{A 3}$$

These values may be used to check whether the theoretical solutions for barge responses are potentially in error as a result of poor numerical conditioning. For the models discussed here $a/b = 3.0$, $a/h = 11.43$, and the lowest irregular frequency is given by $(\omega_{11}^2 a/h) = 12.14$.

REFERENCES

Bendat, J. S. & Piersol, A. G. 1971 *Random Data: Analysis and Measurement Procedures.* Wiley-Interscience.

Brown, D. T. & Patel, M. H. 1981 An investigation of vortex shedding below the keel of a floating offshore vessel in waves. In *Proc. IUTAM Symp. on Unsteady Turbulent Shear Flows* (ed. R. Michel, J. Cousteix & R. Houdeville), p. 329. Springer.

Eatock Taylor, R. 1982 Analysis of hydrodynamic loads by boundary element methods. In *Developments in Boundary Element Methods* – 2 (ed. P. K. Banerjee & R. P. Shaw), p. 211. Applied Science Publishers.

Eatock Taylor, R. & Waite, J. B. 1978 The dynamics of offshore structures evaluated by boundary integral techniques. *Int. J. Num. Meth. Engng* **13**, 73.

Eatock Taylor, R. & Zietsman, J. 1981 Implementation of coupled formulations for hydrodynamic analysis in three dimensions. In *Numerical Methods for Coupled Problems* (ed. E. Hinton, P. Bettess & R. W. Lewis), p. 281. Pineridge.

John, F. 1950 On the motion of floating bodies. II. *Communs Pure Appl. Maths* **3**, 45.

Mei, C. C. 1978 Numerical methods in water wave diffraction and radiation. *Ann. Rev. Fluid Mech.* **10**, 393.

Newman, J. N. 1977 *Marine Hydrodynamics.* M.I.T. Press.

Patel, M. H. & Brown, D. T. 1981 The calculation of vorticity effects on the motion response of a flat-bottomed barge to waves. In *Proc. Intl Symp. on Hydrodynamics in Ocean Engng, Norwegian Inst. of Tech., Trondheim*, 24–28 *August*, p. 667.

Shaw, R. P. 1979 Boundary integral equation methods applied to wave problems. In *Developments in Boundary Element Methods* – 1 (ed. P. K. Banerjee & R. Butterfield), p. 121. Applied Science Publishers.

Ursell, F. 1981 Irregular frequencies and the motion of floating bodies. *J. Fluid Mech.* **105**, 143.